Engineering Applications of Artificial Intelligence 172 (2026) 114302

Contents lists available at ScienceDirect

Engineering Applications of Artificial Intelligence

journal homepage: www.elsevier.com/locate/engappai

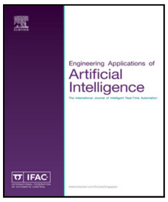

Research paper

A deep learning based method for reference-free full-field strain measurement

Marco Rossi *, Giulia Tanoni, Veronica Ilari, Marco Sasso, Emanuele Principi

Università Politecnica delle Marche, Via Brecce Bianche 12, 60131 Ancona, Italy

ARTICLE INFO

Keywords:
Strain measurement
Deep learning
Reference-free measurement
Digital Image Correlation
Experimental mechanics

ABSTRACT

In this work, we address the problem of estimating full-field planar strain when a reference image of the undeformed configuration is not available. Classical Digital Image Correlation (DIC) and related image-based methods rely on the comparison between undeformed and deformed states and therefore cannot be applied in such scenarios. To overcome this limitation, we propose a deep learning-based approach that estimates the in-plane strain state directly from a single deformed image. A Convolutional Neural Network is trained to regress the two principal strains and their orientation by learning deformation-induced texture features, formulating strain estimation as a data-driven regression problem. The method is validated using synthetically deformed images generated from both classical DIC speckle patterns and steel microstructure images acquired by optical microscopy. A systematic sensitivity analysis is performed to assess the influence of subset size and training dataset size. On synthetic data, the proposed approach achieves coefficients of determination exceeding 0.96 and average strain errors on the order of 0.01 m/m. Preliminary validation on real experimental images of deformed patterns demonstrates that the method can capture meaningful strain distributions, although with lower precision than reference-based DIC, as expected from a statistical, reference-free formulation. The proposed approach is therefore not intended to replace classical DIC, but to enable strain estimation in experimental situations where reference configurations are unavailable.

1. Introduction

Digital Image Correlation (DIC) is currently one of the most widely used methods to measure the displacement and strain field along the surface of solids (Sutton et al., 2009). The fundamental principle of DIC involves comparing a reference image of an object in its undeformed state to images captured during deformation.

DIC allows the measurement of strain on both 2D and 3D surfaces using stereo-DIC. Further set-ups include the use of multiple cameras (Malowany et al., 2017), the use of prisms or other devices to extend the view of a single camera (Genovese et al., 2013), and the possibility of obtaining a 360° measurement of the strain over a component using a rotating camera (Genovese et al., 2016), among others. DIC can be applied to measure extremely small fields of view, e.g., the plastic deformation of a grain Vermeij and Hoefnagels (2018), Vermeij et al. (2022), as well as extremely large ones, e.g., the displacement of the Earth's surface from satellites (Rosu et al., 2015; Aati et al., 2022). Recently, Digital Volume Correlation (DVC) and other techniques have been introduced to obtain the full three dimensional deformation inside a solid (Pan and Wang, 2020; Rossi et al., 2018).

DIC has numerous applications, especially in material characterization (Avril et al., 2008), where it can be used to augment the information achievable from a mechanical test; see, for instance, the Material Testing 2.0 approach (Pierron and Grédiac, 2021). It is also becoming a fundamental tool to compare numerical analysis, for instance with finite element models, and experimental results (Lava et al., 2020).

Recently, given the advancement of Deep Learning (DL) in many domains from time series (Tanoni et al., 2022, 2024) to images processing (Trigka and Dritsas, 2025), and solid mechanics (Hildebrand et al., 2025), researchers have increasingly explored its potential to enhance DIC (Duan et al., 2023; Hassan, 2019) and to develop new applications involving DIC and DL, for instance, in damage detection (Pitz et al., 2023). Convolutional Neural Networks (CNNs), a class of DL architectures suitable for image analysis due to their inherent ability to automatically learn relevant spatial features, have become a natural choice for this exploration. For example, Boukhtache et al. (2021) proposed CNNs as an alternative to traditional correlation algorithms for measuring displacement and strain, reporting improvements in speed and accuracy. Their approach aims to replicate the classical DIC

---

* Corresponding author.
E-mail address: m.rossi@univpm.it (M. Rossi).

https://doi.org/10.1016/j.engappai.2026.114302
Received 23 August 2025; Received in revised form 13 February 2026; Accepted 22 February 2026

process, which involves comparing a reference (undeformed) image with the deformed one to infer deformation. Subsequent work includes both supervised (Duan et al., 2023) and unsupervised (Wang and Zhou, 2024) CNN-based methods for 2D DIC, as well as extensions to stereo-DIC, such as Stereo-DICNet (Feng and Wang, 2024), which employs a unified speckle matching network.

This work introduces a deep learning-based approach for planar deformation assessment. Instead of training a neural network to replicate the traditional DIC process of comparing deformed and undeformed images, we propose and develop a DL-based approach capable of estimating the deformation level *directly and solely* from the deformed image itself. To the best our knowledge, this is the first time that a similar attempt is presented in the literature. A similar concept has recently been used in microfluidic applications to measure the orientation and 3D position of microswimmers from their defocus images (Barnkob et al., 2021; M. Mehdizadeh Youshanlouei, 2024), but it has not yet been applied in DIC. This shift away from image correlation eliminates the requirement for a reference image, thereby unlocking the potential for deformation analysis in previously inaccessible scenarios. For instance, when analyzing material deformation from micrographs of the microstructure, usually only images of the material after deformation are accessible.

To demonstrate the viability of this paradigm, we developed a specific implementation which we call *DeepStrainNet*. Specifically, this first version of DeepStrainNet, presented here, is based on the VGG-16 architecture (Simonyan and Zisserman, 2015). Since the publication of AlexNet (Krizhevsky et al., 2017), a wide variety of CNN architectures have been proposed, including Inception v1 (Szegedy et al., 2014), VGGNets (Simonyan and Zisserman, 2015), ResNet (He et al., 2015), SqueezeNet (Hu et al., 2018), and more recently, MobileNet (Howard et al., 2017) and ShuffleNet (Zhang et al., 2017). For a recent review of CNNs, refer to Li et al. (2022). Among these high-performance architectures, we chose VGG-16 as it is a well-established CNN and it is recognized for its strong generalization capabilities across diverse tasks and datasets, often matching or exceeding the performance of more complex models (Simonyan and Zisserman, 2015). Its effectiveness stems from its depth, achieved using small (3 × 3) convolutional filters. The versatility of VGG-16 is demonstrated by its successful application in numerous fields, including medical image analysis (Shamshad et al., 2024; Kumar and Kumar, 2024; Yadav and Jadhav, 2019; Klangbunrueang et al., 2025; Ankita, 2024), solar panel surface defect detection (Liang et al., 2024), soybean protein identification (Sun et al., 2024), concrete crack detection (Dung and Anh, 2019), plant disease severity estimation (Wang et al., 2017), keyway angle identification (Sarker et al., 2023), satellite applications (Fatima and Soliman, 2025) and many others.

The outline of the paper is as follows. Section 2 describes in detail the proposed method and the used CNN architecture. Section 3 presents the numerical validation of the method, achieved using synthetically deformed images. Section 4 applies the method to two real-world scenarios. Finally, Section 5 discusses the main findings and limitations of the paper, and Section 6 draws the conclusions and outlines future developments.

2. Methods

In standard subset-based DIC, the displacement field is obtained by performing a matching between two speckle patterns, i.e., considering a pixel and its neighborhood in the undeformed image and searching for the same subset in the deformed image, by minimization of a similarity criterion. The strain field is not directly measured, but retrieved through spatial differentiation of the displacement field. In contrast, our work addresses the task of estimating the strain field directly from a single deformed image, using an artificial neural network trained to recognize the deformation of a specific pattern.

A planar deformation field can be expressed in terms of the principal strains (ε_1, ε_2) and the orientation θ of the principal directions, all of which can assume continuous values. Those three variables represent the output of our problem that, accordingly, is framed as a regression task for the DL algorithm. The network takes as input an image $\mathbf{X} \in \mathbb{R}^{N\times M\times C}$, where N and M represent the height and width, respectively, and C denotes the number of channels. In the present application we only consider gray level images, thus $C = 1$. In analogy with DIC, from now on we will refer to the input image $\mathbf{X}$ as "subset". The output of the network is $\mathbf{d} = [\varepsilon_1, \varepsilon_2, \theta]^T$, i.e., an estimate of the principal strain and orientation. Mathematically, the network implements a function $\mathbf{f}_{\boldsymbol{\Theta}} : \mathbb{R}^{N\times M\times C} \rightarrow \mathbb{R}^{3\times 1}$ with trainable parameters $\boldsymbol{\Theta}$ that maps from the input image space to the three output values, i.e.,

$$\mathbf{d} = \mathbf{f}_{\boldsymbol{\Theta}}(\mathbf{X}). \tag{1}$$

The subsequent section delves into the detailed architecture of the neural network used to represent the function $\mathbf{f}_{\boldsymbol{\Theta}}(\cdot)$.

2.1. Neural network architecture

The function $\mathbf{f}_{\boldsymbol{\Theta}}(\cdot)$ in Eq. (1) is implemented using an artificial neural network. DeepStrainNet is a modification of the VGG-16 architecture, originally proposed for image classification (Simonyan and Zisserman, 2015). We retain the convolutional base of VGG-16 as a feature extractor but replace its original classification head with a new fully connected head tailored for a regression task. The resulting architecture is illustrated in Fig. 1.

The network's feature extractor consists of five convolutional blocks. The first two blocks each contain two convolutional layers, while the subsequent three blocks each contain three convolutional layers. The number of filters in the convolutional layers for the five blocks are 64, 128, 256, 512, and 512, respectively. Each convolutional layer uses small 3 × 3 filters and a Rectified Linear Unit (ReLU) activation function. After each block, a 2 × 2 max-pooling layer with a stride of 2 is applied to reduce the spatial dimensions of the feature maps.

The output feature map from the convolutional part is flattened and fed into a custom regression head composed of three fully connected layers. The first two fully connected layers contain 4096 neurons each, designed to capture complex relationships within the extracted features. The final layer is the output layer, which differs significantly from the original VGG-16. Instead of a 1000-neuron softmax layer for classification, our output layer consists of three neurons with a linear activation function. These three neurons directly output the estimated values for the three deformation parameters, $\mathbf{d} = [\varepsilon_1, \varepsilon_2, \theta]^T$, thus performing the regression task.

2.2. Learning

The trainable parameters $\boldsymbol{\Theta}$ of the DeepStrainNet network are optimized by training the model on a labeled dataset. Given a dataset of input subsets $\mathcal{X} = \{\mathbf{X}_i\}_{i=1}^N$ and their corresponding ground truth deformation parameters $\mathcal{D} = \{\mathbf{d}_i\}_{i=1}^N$, where $\mathbf{d}_i = [\varepsilon_{1i}, \varepsilon_{2i}, \theta_i]^T$, the network is trained by minimizing the Mean Squared Error (MSE) loss function:

$$L(\boldsymbol{\Theta}) = \frac{1}{N}\sum_{i=1}^{N} \|\mathbf{f}_{\boldsymbol{\Theta}}(\mathbf{X}_i) - \mathbf{d}_i\|^2, \tag{2}$$

where $\|\cdot\|^2$ denotes the Euclidean norm squared.

Training is performed using the Adam optimizer (Kingma and Ba, 2015) with hyperparameters $\beta_1 = 0.9$ and $\beta_2 = 0.999$. To improve the learning process, a dynamic learning rate was employed based on the cosine decay strategy (Loshchilov and Hutter, 2017). In this approach, the learning rate is gradually decreased over the training steps, following a cosine curve. The expression for the cosine decay learning rate is the following:

$$\eta(t) = \eta_{min} + \frac{1}{2}(\eta_{max} - \eta_{min})\left[1 + \cos\left(\pi\frac{t}{T}\right)\right], \tag{3}$$

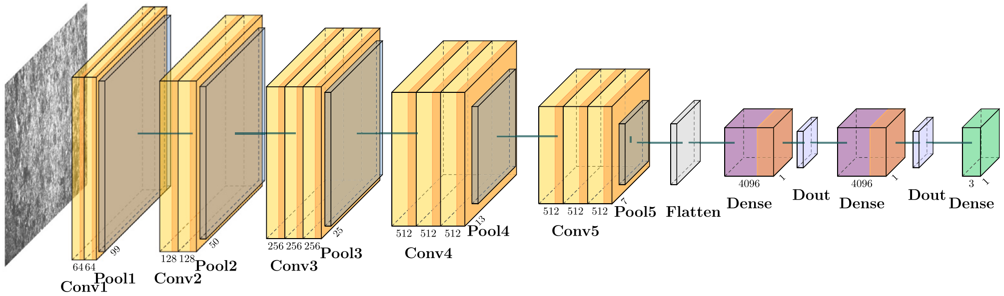

Fig. 1. The proposed neural network architecture. Differently from the standard VGG-16 architecture, the last layer has 3 outputs, one for each deformation parameter ($\varepsilon_1, \varepsilon_2, \theta$), and a linear activation function. *Conv* refers to the convolutional layers, *Pool* refers to the pooling layers, *Dense* to the fully connected layers and *Dout* refers to the dropout layer.

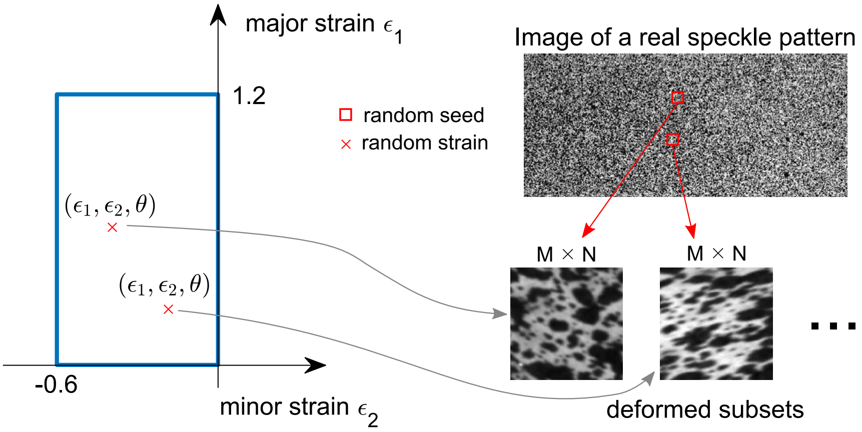

Fig. 2. Generation of deformed subsets for training and validation purposes from a high-resolution image. Random sampling is used to populate the strain domain and select different speckle patterns.

where $\eta(t)$ is the learning rate at the current training step t, η_{min} is the minimum learning rate, η_{max} is the maximum learning rate, and T is the total number of training steps. The specific values used for the learning rate and other training hyperparameters will be presented in Section 3.

3. Numerical validation

We first demonstrate a proof of concept for DeepStrainNet using synthetic images. The images were generated using a simulator able to reproduce realistic deformed images including experimental uncertainties (noise, changes of illumination, lens distortion, etc.) (Rossi et al., 2015). This is nowadays often referred to as a Digital Twin (DT) of a real test and it is used in the experimental mechanics community to evaluate the uncertainties of new identification or measurement methods (Badaloni et al., 2015; Peshave et al., 2024). Synthetic images are also consistently used to evaluate the performance of DIC algorithms and to perform benchmarking, see, for instance, the DIC challenge (Reu et al., 2018).

3.1. Synthetic image generation

The image generation process follows the principle of optical flow conservation. An image can be described as a continuous function $I(\mathbf{r})$ of the gray level with respect to the position vector $\mathbf{r}$, defined over a spatial domain that represents the image size. Let $I_0(\mathbf{r})$ denote the reference image function and $I_d(\mathbf{r})$ the deformed image, distorted according to a material transformation function χ. According to the optical flow conservation principle, we have:

$$I_d(\mathbf{r}) = I_0\left(\chi^{-1}(\mathbf{r})\right). \tag{4}$$

This principle can be used to deform any image according to a given deformation field $\mathbf{u}$ (Rossi and Pierron, 2012), as follows:

$$\chi = \mathbf{r} + \mathbf{u}(\mathbf{r}). \tag{5}$$

The function $I_0(\mathbf{r})$ can be defined either analytically or created from existing reference images using pixel interpolation to make it continuous. More details can be found in Rossi and Pierron (2012). In this study, $I_0(\mathbf{r})$ is obtained via cubic interpolation of an 8-bit reference image. Eq. (5) is then used to generate subsets of $N \times M$ pixels with an assigned level of deformation, expressed in terms of ε_1, ε_2 and θ. The level of deformation within the subset is constant and can be generated using the following analytical displacement field $\mathbf{u}(x, y)$:

$$\begin{aligned} u(x, y) &= (e^{\varepsilon_1} + 1)\cos\theta\, x \;-\; (e^{\varepsilon_2} + 1)\sin\theta\, y, \\ v(x, y) &= (e^{\varepsilon_1} + 1)\sin\theta\, x \;+\; (e^{\varepsilon_2} + 1)\cos\theta\, y. \end{aligned} \tag{6}$$

with x and y being the Cartesian coordinates.

The procedure for generating the synthetic subsets is illustrated in Fig. 2.

First, a random level of deformation is selected in terms of ε_1, ε_2 and θ. The parameters are constrained within the following ranges:

$$\begin{aligned} &\varepsilon_1 \in [0,\ 1.2], \\ &\varepsilon_2 \in [-0.6,\ 0], \\ &\theta \in \left[-25^\circ,\ +25^\circ\right]. \end{aligned} \tag{7}$$

These ranges correspond to a tensile and shear-dominated type of stress, i.e., the top-left quadrant of the principal strain diagram shown in Fig. 2. For larger rotation ranges, the direct regression of θ may lead to ambiguities due to symmetry in the deformation-induced features; in such cases, a trigonometric representation based on $(\sin\theta, \cos\theta)$ could improve robustness.

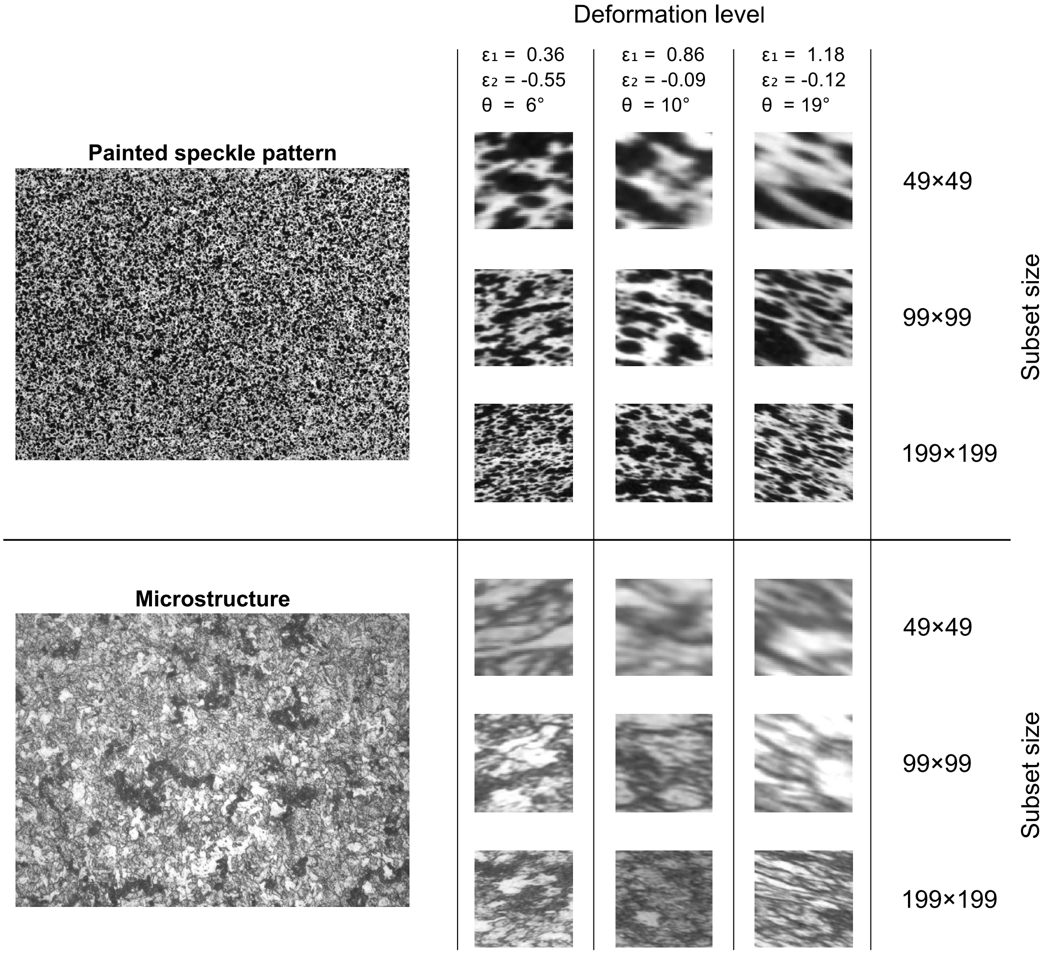

Fig. 3. Examples of the subsets generated for training. Different deformation levels and subset sizes are illustrated. Two types of high-resolution images are used: speckle pattern and microstructure, respectively.

Afterwards, a random seed point is selected within a high-resolution reference image of an undeformed pattern. Finally, the DT is used to generate a deformed subset of $N \times M$ pixels centered at the seed point. Possible experimental uncertainties were introduced through the digital twin. In particular, a random gray-level noise with a standard deviation of 4 gray levels and a random illumination variation with a maximum amplitude of 10% with respect to the average illumination were applied.

This process allows for the generation of thousands of mostly independent subsets, starting from a few high resolution reference images of the investigated pattern, as both the deformation level and the local features of pattern are varied randomly. Examples of the generated subsets are illustrated in Fig. 3 for different levels of deformation and subset sizes.

In this paper, we study two types of patterns: a classical white-light speckle pattern used in DIC applications, created using black and white spray paint, and the microstructure pattern of an X65 steel sample obtained through optical microscopy. The image used to generate the speckle-pattern subsets has a resolution of 2160 × 4096 pixels, whereas ten micrographs with a resolution of 1536 × 2048 pixels each were employed to create the microstructure-based patterns.

3.2. Sensitivity analysis and training configuration

To identify the optimal input image size and training dataset size for DeepStrainNet, we conducted a systematic sensitivity analysis. This analysis was performed using the microstructure pattern dataset, which represents the more challenging scenario due to its complex and variable features.

The synthetically generated dataset of subsets was divided into training, validation, and test sets by creating orthogonal sets from different images. This approach ensures that the images used for training are distinct from those in the test set.

The performance of the model for each configuration was evaluated using the coefficient of determination, R^2, a widely recognized metric for evaluating regression models (Chicco et al., 2021). This metric measures the extent to which the variation in a dependent variable y is explained by the independent variables in the model. Values closer to 1 indicate a better fit, meaning the model is more likely to make accurate predictions for unseen data. R^2 is calculated as follows:

$$R^2 = 1 - \frac{\sum_{i=1}^{n}(d_i - \hat{d}_i)^2}{\sum_{i=1}^{n}(d_i - \bar{d})^2}, \tag{8}$$

where d_i represents a ground truth value, $\hat{d}_i$ is the value predicted by the model, $\bar{d}$ is the mean of the ground truth values, and n is the total number of samples.

All models in this sensitivity analysis were trained for a maximum of 1000 epochs using the Adam optimizer with a batch size of 64 and a cosine decay learning rate schedule (see Section 2.2), starting from a maximum learning rate of 10^{-4}. An early stopping strategy with a patience of 30 epochs was employed to halt training when the performance on the validation set no longer improved, ensuring the best model was saved. The deep learning method was implemented in Python using the TensorFlow and Keras libraries.

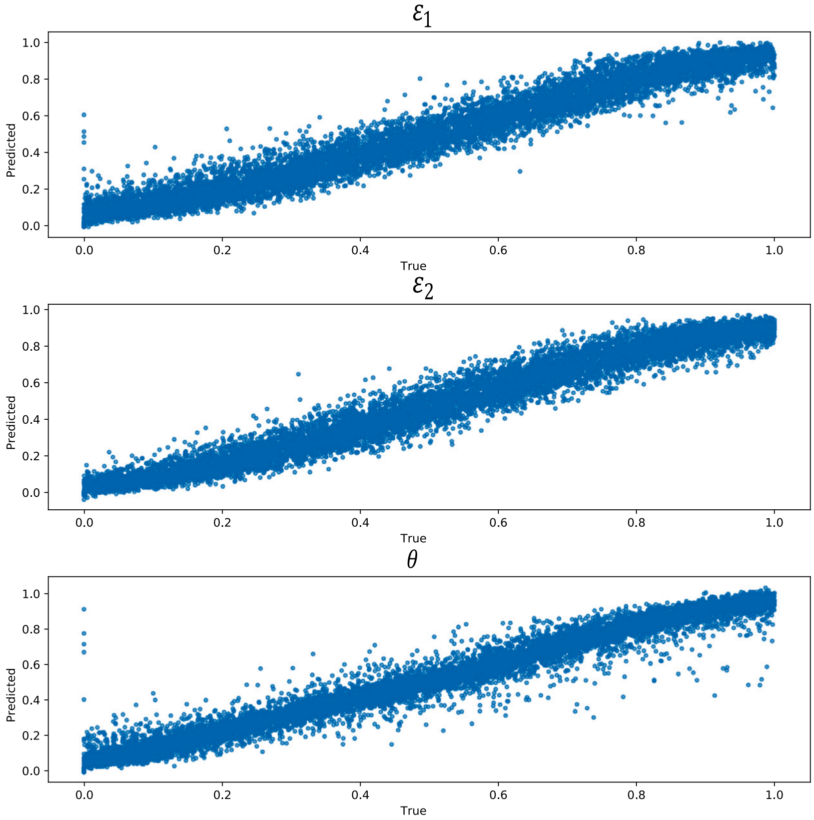

Fig. 4. Scatter plots for the three estimated deformation values and the true values for the optimal configuration (image size 99 × 99, 20,000 training images).

Table 1
Results of the sensitivity analysis in terms of R^2 using the microstructure pattern. Different image sizes and training set sizes are considered. The reported results represent the mean and standard deviation across five different training runs.

Image size	Training set	Validation set	Test set	R^2 on test set			
(pixel)	(# of images)	(# of images)	(# of images)	ε_1	ε_2	θ	Average
49 × 49	5000	1000	1000	0.506 ± 0.033	0.895 ± 0.008	0.850 ± 0.029	0.750 ± 0.023
99 × 99	5000	1000	1000	0.718 ± 0.031	0.953 ± 0.004	0.957 ± 0.026	0.876 ± 0.017
199 × 199	5000	1000	1000	0.759 ± 0.019	0.950 ± 0.007	0.906 ± 0.017	0.872 ± 0.011
99 × 99	30,000	10,000	10,000	0.947 ± 0.002	0.945 ± 0.004	0.965 ± 0.001	0.952 ± 0.003
99 × 99	25,000	10,000	10,000	0.947 ± 0.006	0.953 ± 0.004	0.958 ± 0.003	0.952 ± 0.004
99 × 99	20,000	10,000	10,000	0.936 ± 0.013	0.96 ± 0.001	0.960 ± 0.003	0.952 ± 0.006
99 × 99	15,000	10,000	10,000	0.916 ± 0.029	0.96 ± 0.003	0.950 ± 0.009	0.942 ± 0.014
99 × 99	10,000	10,000	10,000	0.859 ± 0.030	0.953 ± 0.003	0.924 ± 0.008	0.911 ± 0.014
99 × 99	5000	10,000	10,000	0.784 ± 0.020	0.947 ± 0.005	0.896 ± 0.009	0.875 ± 0.011

The results of the sensitivity analysis are summarized in Table 1, which lists the R^2 performance for each deformation parameter and the average score on the test set.

We first investigated the impact of image size using a training set of 5000 images and validation and test sets of 1000 images each. Three image sizes were considered: 49 × 49, 99 × 99, and 199 × 199. A significant improvement in the average R^2 is observed when increasing the image size from 49 × 49 to 99 × 99 pixels. However, further enlarging the images to 199 × 199 did not yield a notable benefit, with the drawback of increasing the computational load. This can be explained qualitatively by observing the examples in Fig. 3; the texture features in a 49 × 49 subset are rather heterogeneous, while they already appear nearly homogeneous in the 99 × 99 subset. It is worth noting that this optimal size is much larger than the subset size commonly used in standard DIC applications, i.e., 15–21 pixels, which is reasonable given that our method operates without a reference image.

After identifying 99 × 99 pixels as the optimal image size, the amount of training data was varied to find the best-performing model. As shown in Table 1, accuracy improves considerably as the training set size increases from 5000 (average $R^2 = 0.88$) to 20,000 images (average $R^2 = 0.952$). Beyond this point, performance stabilizes and shows a slight decrease, suggesting that the network may begin to overfit despite the early stopping mechanism. Based on this analysis, an image size of 99 × 99 pixels and a training set of 20,000 images were selected as the optimal configuration. Across all tests, the major strain ε_1 consistently appears to be the most challenging parameter for the network to identify accurately.

Finally, this optimal configuration (image size 99 × 99, 20,000 training images) was used to train and test a new model on sub-images derived from the speckle pattern. An example of the obtained scatter plot is illustrated in Fig. 4. A comparison of the performance on both datasets is graphically shown in Fig. 5. The performance is very similar for both patterns, with the minor strain ε_2 being estimated slightly better for the speckle pattern ($R^2 = 0.98$ vs. 0.96). It must be noted, however, that such findings are specific to the patterns used in this study; a different optimal configuration may be required for new patterns.

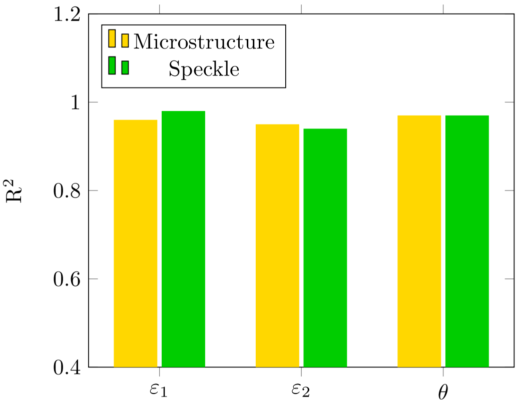

Fig. 5. Comparison of the R^2 values for the optimal configuration on the microstructure and speckle pattern datasets.

3.3. Computational cost

The proposed neural network has a computational complexity of 5.78 GFLOPs and 2.89 G MACC, estimated using a Python script (available at the project repository) and TensorFlow's native profiling functions. The average inference time per image is approximately 0.007 s. During training, the network requires about 15 s per epoch (≈47 ms per step), yielding a total training time of roughly 28 min under optimal conditions; this may vary with dataset configuration because of the early stopping criterion. All experiments were performed on an NVIDIA DGX A100. Once the CNN is trained, it can be used to estimate strain fields in real images with a computational time comparable to that of classical DIC on standard laptops.

3.4. Validation on constant strain fields

Using the optimal configuration identified in the previous section (99 × 99 pixel images, 20,000 training samples), the performance of DeepStrainNet was evaluated on two canonical test cases: a constant, uniform strain field and a spatially varying sinusoidal strain field. For the first test, the DT was used to generate a deformed image of 1600 × 1600 pixels, applying a constant deformation. The target deformation is $\varepsilon_1 = 0.3$, $\varepsilon_2 = -0.1$, and $\theta = 5°$. A Gaussian gray-level noise with a standard deviation of 5 gray levels was added to assess the model's robustness to measurement noise. DeepStrainNet was then used in the deformed image similarly to a DIC software, with a subset of 99 × 99 pixels and a step size of 32 pixels. Accordingly, it is possible to extract the predicted strain field, directly from the deformed image using the trained CNN.

Fig. 6 shows the strain maps obtained with DeepStrainNet for the two investigated patterns. Each plot also reports on top the corresponding mean and standard deviation. In the contour bands, the red color represents the target value and the yellow indicates an interval of ± 0.01. As a general remark, the results on the speckle pattern are more precise than those on the microstructure. For the speckle pattern, the strain reconstruction error in terms of both bias and standard deviation is around 0.01. For the microstructure, the bias is larger, especially for the major strain ε_1. However, looking at the contour maps, it is clear that the error is not homogeneous across the image but rather there are zones that are consistently poorly estimated. This is better investigated in Fig. 7, where the deformed image used to obtain the test set is shown as well as the mean absolute relative error (MARE) of the principal strains. From this figure, it is evident that the red zone, where the prediction is incorrect, corresponds to a region where the microstructure pattern is not suitable. Conversely, in the green area, where the prediction is accurate, the pattern appears almost regular. The orange zone, instead, is more difficult to interpret, as a poor estimation is observed only for the major strain ε_1, even though the microstructure pattern looks very similar to that in the green zone.

An in-depth sensitivity analysis of the DeepStrainNet parameters is beyond the scope of this paper. However, an indication of the effect of the step size can be inferred from the analysis shown in Fig. 8. Here, the principal strain ε_1 is evaluated along a single pixel line extracted from the center of the deformed image of the speckle pattern. Different step sizes are used, namely 1, 32 (which is the value adopted in the previous analyses), and 99, corresponding to the subset size. The results show that reducing the step size does not lead to significant variations in the predicted strain field, since no additional information is introduced due to the overlap between neighboring subsets. This behavior is analogous to what is commonly observed in classical DIC analyses.

3.5. Validation on strain gradients

For the second test case, we evaluated the capability of DeepStrainNet to retrieve strain gradients in one direction. In this case, we applied

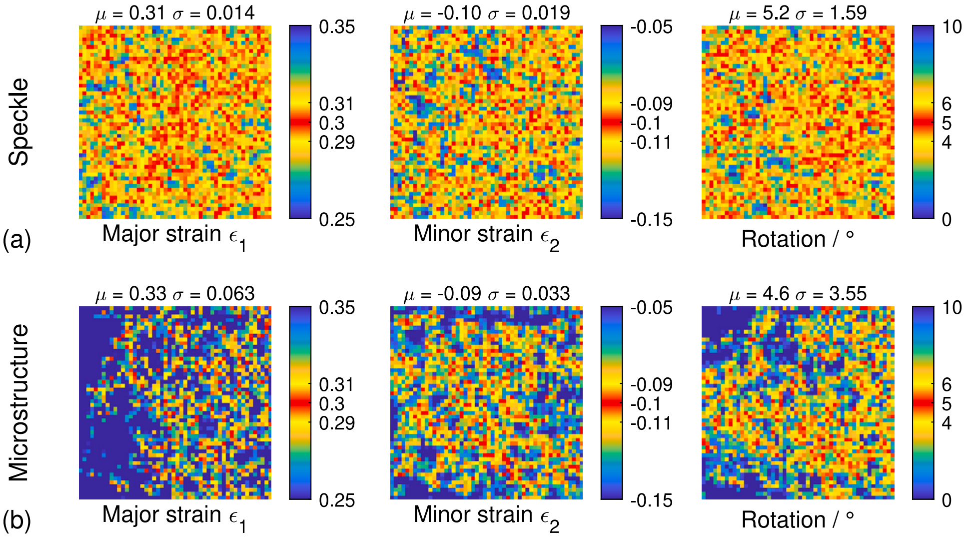

Fig. 6. Strain maps obtained with DeepStrainNet for the constant strain test, using (a) the speckle pattern and (b) the microstructure as the initial image. The mean μ and standard deviation σ for each map are displayed above it. In the contour bands, the red color represents the target strain value, and yellow indicates an interval of ± 0.01 around the target.

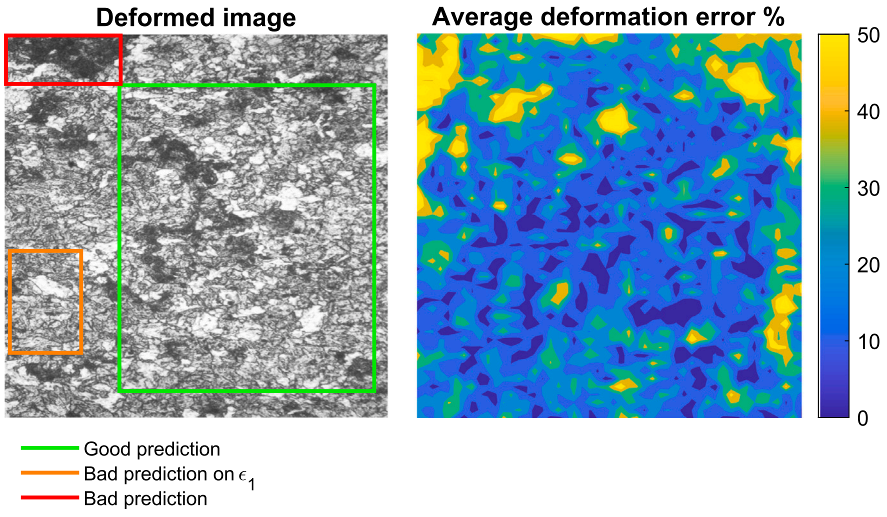

Fig. 7. Deformed image of the microstructure used to create the test set analyzed in Fig. 6. The quality of the prediction is illustrated by the mean absolute relative error of the principal strains, map on the right.

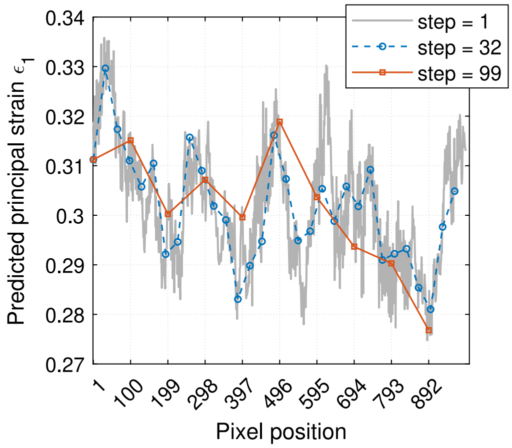

Fig. 8. Influence of different step sizes.

a sinusoidal strain gradient in the horizontal direction x, going from 0 to a maximum value ϵ_1, while keeping the other components at zero. Such a strain field can be generated using Eq. (5) with the following displacement function:

$$u(x,y) = \frac{(e^{\epsilon_1}+1)}{2}x + \frac{(e^{\epsilon_1}+1)\,p}{4\pi}\sin\left(\frac{2\pi x}{p}\right),$$

$$v(x,y) = 0. \tag{9}$$

where p is the spatial period of the sine function in pixels. A reference image is deformed according to this transformation, then subsets of 99 × 99 pixels were extracted every 32 pixels and used as a test set. The results are shown in Fig. 9, where only the map for ϵ_1 is shown. Qualitatively, DeepStrainNet is able to reconstruct the deformation gradient. In the plots on the right, the blue line represents the theoretical deformation applied to the image, and the red dots are the predictions from the network. The error level observed with gradients is larger than that observed in the previous case with constant fields. Moreover, the predictions tend to underestimate the target value, though the reason for this is not yet fully understood. It must be underlined that this condition is particularly severe because a strong gradient is applied, meaning the deformation within a 99 × 99 sub-image is not constant, whereas the network was trained exclusively on constant strain fields. Nonetheless, DeepStrainNet is still able to reconstruct the overall trend, demonstrating the robustness of the method. Strain gradients could also be included in the training set but this is beyond the scope of this paper.

4. Application to experimental images

After validating the proposed method using synthetic data, we applied DeepStrainNet to real experimental images of deformed samples. The same patterns studied previously are considered, i.e., the white light speckle and the microstructure pattern. The two experiments are detailed below.

4.1. Experimental speckle pattern

In this scenario, DeepStrainNet was applied to data from a tensile test conducted on a notched DP600 steel specimen in order to obtain a heterogeneous strain field. The ground-truth deformation field for this experiment was measured using a commercial DIC software (MatchID[1]). This dataset serves as a realistic benchmark for evaluating how well the proposed approach generalizes to actual experimental data.

To ensure a strict separation between training/validation and test sets, the spatial domain of the specimen was divided into non-overlapping regions, as illustrated in Fig. 10. The left side of the specimen was used exclusively to source the training and validation data. The right side was reserved entirely for the test set. This strategy ensures that the model is evaluated on truly unseen pattern, in other words, the level of deformation on the two sides of the specimen is very similar but the random speckle pattern is different.

From five different deformed images corresponding to five distinct load steps of the test, sub-images of 99 × 99 pixels were extracted with a step size of 21 pixels from the left-side region. This process yielded a total of about 50,000 sub-images, which were split into a training set of 40,000 images and a validation set of 10,000. The network was trained using only these deformed images, without any information about the initial undeformed speckle pattern. The test set, consisting of approximately 10,000 sub-images, was generated entirely from a single image of the specimen's right side.

The comparison is shown in Fig. 11. Although the strain field is rather noisy compared to the DIC counterpart, DeepStrainNet is able to correctly capture the strain gradient. The deformation is obtained in each subset independently, and no smoothing is introduced.

---

[1] https://www.matchid.eu

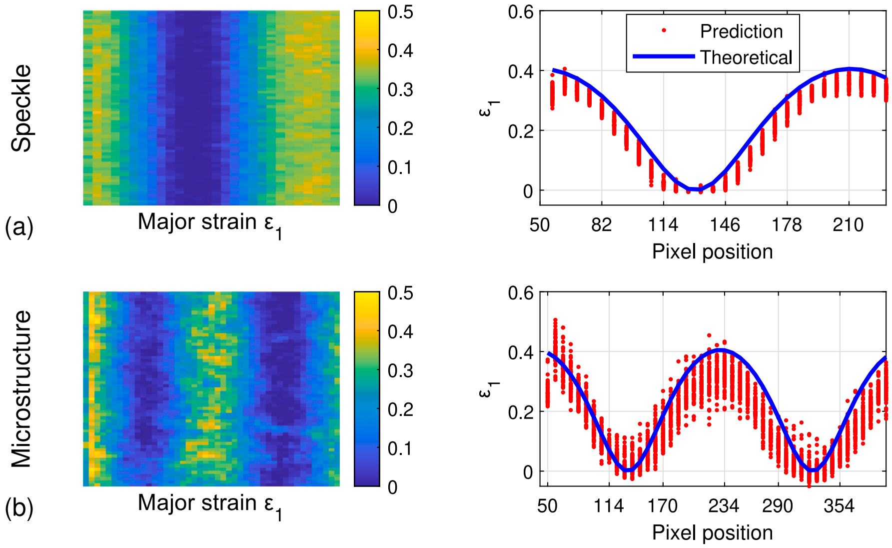

Fig. 9. Major strain ε_1 maps obtained by imposing a sinusoidal displacement, and comparison with the CNN prediction, using (a) the speckle pattern and (b) the microstructure, respectively, as the initial image.

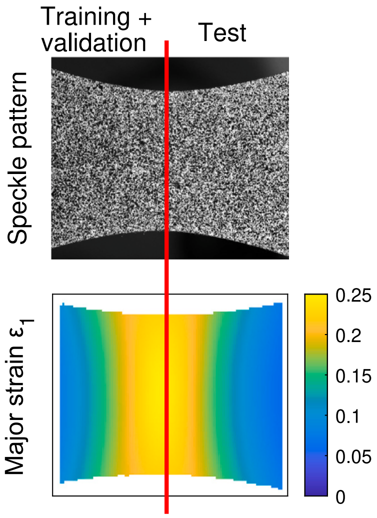

Fig. 10. Spatial division of the real specimen into two subsets: training + validation on the left, testing on the right.

Fig. 11 can be interpreted as a qualitative comparative baseline between classical DIC and DeepStrainNet. Classical DIC provides high-precision strain measurements through the comparison of an undeformed and a deformed configuration, whereas DeepStrainNet estimates the deformation level from a single image and therefore relies on a statistical inference, resulting in lower precision. The relevance of DeepStrainNet lies in scenarios where a reference image is not available and classical DIC cannot be applied.

4.2. Microstructure

The last scenario is defined to evaluate the case where the training set consists of synthetically generated data as described in Section 3.1 with constant and uniform deformation, while the test set contains real data. This case study serves as a feasibility check to assess whether synthetically generated images are informative enough to train a neural network that is then applied to real images.

The subset for the test set are derived from two micrographs taken from a deformed specimen close to the fracture point, as illustrated in Fig. 12. The deformed material is the same X65 steel used in Section 3.1 to create synthetic deformed patterns and train DeepStrainNet. These synthetic patterns were generated starting from a micrograph of the undeformed material, in order to simulate deformation conditions analogous to those observed experimentally.

In this case we do not have a direct measurement of the deformation level in the inspected zone, but we used a FE model of the test to estimate the deformation, see Fig. 13. The FE model was built using ABAQUS/Standard with isotropic plasticity and will not be further discussed here, since it only serves as a general estimate of the deformation level. The expected values are $\varepsilon_1 \approx 0.3$ and $\varepsilon_2 \approx -0.15$, respectively.

Looking at the prediction of the model, the level of deformation of the component ε_2 is retrieved fairly accurately, with an average value of around -0.13 within the red boxes highlighted in the figure. Instead, the major component ε_1 is consistently underestimated. This outcome can be attributed to the discrepancy between the synthetic images used for the training and validation sets and the real micrographs employed in the test set as discussed in the next section. It is worth noting that the second micrograph, Fig. 12b, also includes the resin of the mounted specimen on the right side. This zone is clearly distinguishable in the prediction map, giving evidence that DeepStrainNet is able to properly distinguish whether the deformed pattern is present or not.

5. Discussion

The proposed *DeepStrainNet* approach demonstrates that it is possible to extract meaningful strain information from a single deformed image, without requiring a reference configuration. It is important to note that the method assumes a texture with locally repeatable statistical properties, so that the deformation-induced changes exceed or remain distinguishable from the natural variability of the pattern; when this condition is not met, as in highly irregular or heterogeneous microstructures, the accuracy of reference-free strain estimation will be reduced. The performance on synthetic data is consistent across both standard speckle patterns and real microstructural textures, with high R^2 scores for all deformation components. This confirms the capability of the neural network to regress principal strains and orientation from local texture variations.

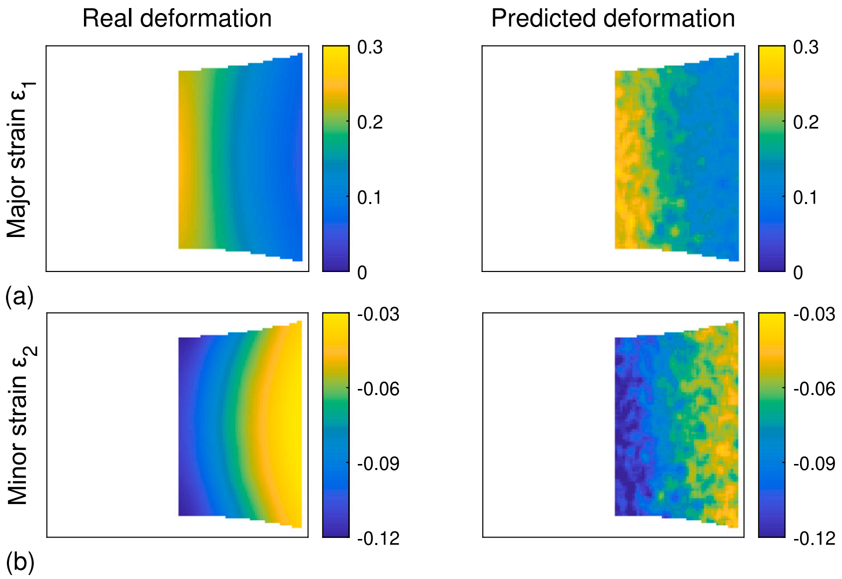

Fig. 11. Comparison between the deformation measured with DIC in the real experiment and the deformation predicted by the CNN, using speckle patterns for (a) major strain ε_1 and (b) minor strain ε_2.

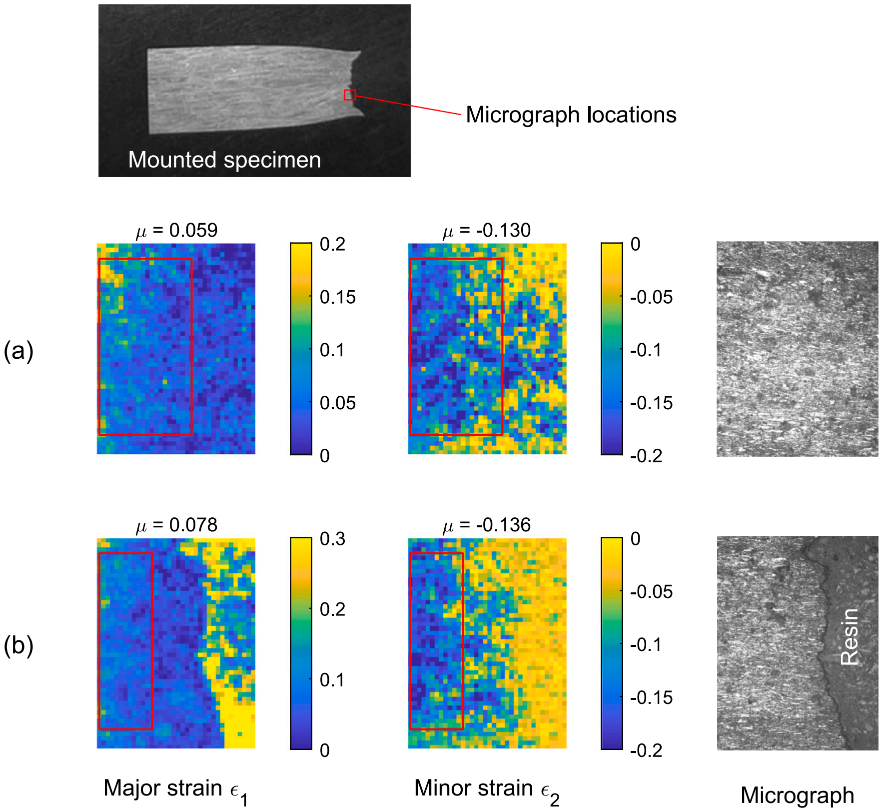

Fig. 12. Strain maps obtained from real deformed microstructure using a CNN trained with a synthetic training set. Two micrographs, (a) and (b), were analyzed.

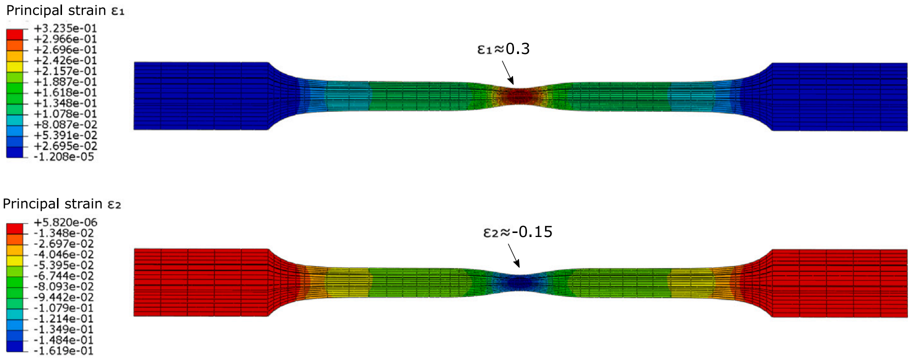

Fig. 13. Finite element model of the tested specimen, from which the sample used for micrography was extracted. The expected strain level can be reasonably estimated by inspecting the central zone, where deformation is maximum.

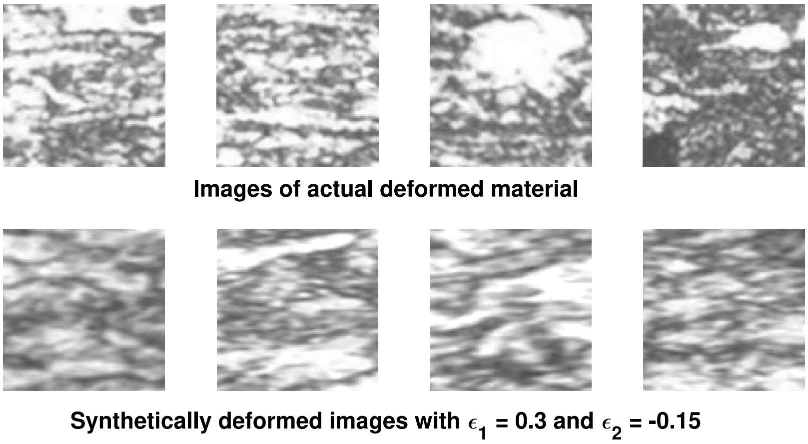

Fig. 14. Comparison between the images of a deformed microstructure used as test set and the synthetically deformed images used as training set.

However, the application to real experimental deformed pattern revealed several limitations when the neural network is trained with synthetic data. While the model successfully identifies deformation regions and yields qualitatively plausible strain maps, quantitative discrepancies were observed. In particular, the estimation of the major strain ε_1 tends to be systematically underestimated, despite acceptable performance on the minor strain ε_2. This behavior is consistent with the sensitivity analysis, where ε_1 was shown to be the most challenging parameter to predict, for this particular pattern.

The critical point is the domain gap between synthetic training data and real microstructure images. Although synthetic images were generated with realistic noise, lighting variations, and distortion, they may still lack the full complexity of actual deformed metallographic textures, including grain boundaries, phase contrast, and topological noise. A comparison between actual and synthetically deformed microstructure is given in Fig. 14. Globally, the shape of the main patterns looks similar but a difference can be clearly observed. The real micrographs have a sharper contrast and the shape of the smallest features is different.

It is worth noting that bridging this domain gap via standard fine-tuning or transfer learning was not feasible in this study due to the specific nature of the available datasets. For the speckle pattern case, since a large dataset of annotated real images was available, training the network from scratch on real data was preferred over fine-tuning a synthetically-trained model on a smaller subset. On the other hand, for the microstructure analysis, accurate ground truth annotations were unavailable. As detailed in Section 4, the FE model provided only a macroscopic estimation for validation purposes, which is insufficient for the supervised learning required by fine-tuning. Therefore, addressing the systematic underestimation in microstructural analysis requires alternative strategies such as unsupervised domain adaptation or improved synthetic data generation.

Despite these limitations, the network was able to distinguish the resin boundary in the mounted sample, suggesting that it learned to recognize valid deformation patterns while ignoring non-informative regions. Moreover, the estimation of the minor strain is already reasonably accurate. We believe these results are very promising, especially considering the significant potential for improvement of the proposed technique.

6. Conclusion

In this study, we introduced DeepStrainNet, a deep learning-based approach for full-field strain estimation from a single deformed image, eliminating the need for a reference configuration. The main findings of the work can be summarized as follows:

- A novel reference-free framework for strain estimation was proposed, demonstrating that the principal strains (ε_1, ε_2) and their orientation (θ) can be inferred directly from a single deformed image using a convolutional neural network. This represents a conceptual departure from classical DIC-based approaches, which inherently rely on a reference configuration.
- The feasibility of the proposed approach was demonstrated through numerical validation on synthetically generated datasets derived from both classical speckle patterns and real microstructural images, showing that meaningful strain information can be extracted from local texture variations.
- Applications to real experimental images confirmed that DeepStrainNet can capture relevant strain distributions even in the

absence of a reference image, albeit with lower precision than classical DIC, as expected from a statistical, reference-free formulation.

While the present validation is limited to specific materials and deformation scenarios, the results still demonstrate the potential of the proposed methodology for experimental situations where reference images are unavailable.

Future works will focus on bridging the domain gap between synthetic and experimental data. First, we may explore domain adaptation techniques, which have been proven effective in bridging the synthetic-to-real gap in both general computer vision tasks (Peng et al., 2018) and specific regression applications (Nejjar et al., 2023). Furthermore, the potential of transfer learning should be investigated (Pan and Yang, 2010). Seminal works have demonstrated that deep neural networks learn hierarchical representations, where early layers capture universal geometric primitives (such as edges and local gradients) that are broadly transferable across visual domains (Yosinski et al., 2014; Donahue et al., 2014). In our context, this suggests that the pre-trained model could serve as a robust feature extractor for new material textures, allowing for efficient fine-tuning with minimal experimental data. Additionally, the use of more diverse training datasets obtained from generative models (Fokina et al., 2020; Karras et al., 2019) or augmented images, and hybrid loss functions that incorporate spatial smoothness or physical constraints could be investigated. Finally, moving from patch-wise prediction to context-aware architectures, such as encoder–decoder models or attention-based networks, could better capture deformation trends across larger spatial scales and handle multi scale strain analysis.

CRediT authorship contribution statement

Marco Rossi: Writing – original draft, Supervision, Methodology, Formal analysis, Data curation, Conceptualization. **Giulia Tanoni:** Writing – original draft, Validation, Software, Methodology, Investigation, Data curation. **Veronica Ilari:** Writing – original draft, Visualization, Validation, Investigation, Data curation. **Marco Sasso:** Writing – review & editing, Supervision, Funding acquisition. **Emanuele Principi:** Writing – original draft, Supervision, Project administration, Methodology, Funding acquisition, Formal analysis, Conceptualization.

Declaration of competing interest

The authors declare that they have no known competing financial interests or personal relationships that could have appeared to influence the work reported in this paper.

Acknowledgments

This research has received funding from the project Sustainable Mobility Center – Project Code CN00000023, CUP I33C22001240001 - funded under the National Recovery and Resilience Plan (NRRP), Mission 4 Component 2 Investment 1.4 - Enhancement of research structures and establishment of “national champions” in R&D on selected Key Enabling Technologies “Sustainable Mobility Center (Centro Nazionale per la Mobilità Sostenibile – CNMS)” Call for tender No. 3138 of 16/12/2021, and Concession Decree No. 0001033.17-06-2022 of Italian Ministry of University funded by the European Union – NextGenerationEU. The opinions expressed are those of the authors only and should not be considered representative of the European Union or the European Commission’s official position. Neither the European Union nor the European Commission can be held responsible for them.

Data availability

Data will be made available on request.

References

Aati, S., Milliner, C., Avouac, J.-P., 2022. A new approach for 2-d and 3-d precise measurements of ground deformation from optimized registration and correlation of optical images and ica-based filtering of image geometry artifacts. Remote Sens. Environ. 277, 113038.

Ankita, S. Mittal, 2024. Image classification of satellite using VGG16 model. In: Proceedings of the 2024 2nd International Conference on Disruptive Technologies. ICDT, IEEE, Greater Noida, India, pp. 401–404.

Avril, S., Bonnet, M., Bretelle, A.-S., M. Grédiac, F. Hild, Ienny, P., Latourte, F., Lemosse, D., Pagano, S., Pagnacco, E., et al., 2008. Overview of identification methods of mechanical parameters based on full-field measurements. Exp. Mech. 48, 381–402.

Badaloni, M., Rossi, M., Chiappini, G., Lava, P., Debruyne, D., 2015. Impact of experimental uncertainties on the identification of mechanical material properties using DIC. Exp. Mech. 55, 1411–1426.

Barnkob, R., Cierpka, C., Chen, M., Sachs, S., P. Mäder, M. Rossi, 2021. Defocus particle tracking: a comparison of methods based on model functions, cross-correlation, and neural networks. Meas. Sci. Technol. 32 (9), 094011.

Boukhtache, S., Abdelouahab, K., Berry, F., Blaysat, B., M. Grédiac, F. Sur, 2021. When deep learning meets digital image correlation. Opt. Lasers Eng. 136, 106308.

Chicco, D., Warrens, M.J., Jurman, G., 2021. The coefficient of determination r-squared is more informative than smape, mae, mape, mse and rmse in regression analysis evaluation. PeerJ Comput. Sci. 7, 1–24.

Donahue, J., Jia, Y., Vinyals, O., Hoffman, J., Zhang, N., Tzeng, E., Darrell, T., 2014. Decaf: A deep convolutional activation feature for generic visual recognition. In: International Conference on Machine Learning. pp. 647–655.

Duan, X., Xu, H., Dong, R., Lin, F., Huang, J., 2023. Digital image correlation based on convolutional neural networks. Opt. Lasers Eng. 160, 107234.

Dung, C.V., Anh, L.D., 2019. Autonomous concrete crack detection using deep fully convolutional neural network. Autom. Constr. 99, 52–58.

Fatima, T., Soliman, H., 2025. Application of vgg16 transfer learning for breast cancer detection. Information 16 (3), 227.

Feng, Y., Wang, L., 2024. Stereo-dicnet: An efficient and unified speckle matching network for stereo digital image correlation measurement. Opt. Lasers Eng. 179, 108267.

Fokina, D., Budennyy, S., Korolev, V., Safonov, A., Oseledets, I., 2020. Microstructure synthesis using style-based generative adversarial networks. In: Proceedings of the IEEE/CVF Conference on Computer Vision and Pattern Recognition Workshops. pp. 858–859.

Genovese, K., Casaletto, L., Rayas, J., Flores, V., Martinez, A., 2013. Stereo-digital image correlation (DIC) measurements with a single camera using a biprism. Opt. Lasers Eng. 51 (3), 278–285.

Genovese, K., Cortese, L., Rossi, M., Amodio, D., 2016. A 360-deg digital image correlation system for materials testing. Opt. Lasers Eng. 82, 127–134.

Hassan, G.M., 2019. Discontinuous and pattern matching algorithm to measure deformation having discontinuities. Eng. Appl. Artif. Intell. 81, 223–233. http://dx.doi.org/10.1016/j.engappai.2019.02.017.

He, K., Zhang, X., Ren, S., Sun, J., 2015. Deep residual learning for image recognition. arXiv:1512.03385 https://arxiv.org/abs/1512.03385.

Hildebrand, S., Friedrich, J.G., Mohammadkhah, M., Klinge, S., 2025. Coupled CANN-DEM simulation in solid mechanics. Mach. Learn. : Sci.Technol. 6, 015038.

Howard, A.G., Zhu, M., Chen, B., Kalenichenko, D., Wang, W., Weyand, T., Andreetto, M., Adam, H., 2017. Mobilenets: Efficient convolutional neural networks for mobile vision applications. arXiv:1704.04861 https://arxiv.org/abs/1704.04861.

Hu, J., Shen, L., Sun, G., 2018. Squeeze-and-excitation networks. In: 2018 IEEE/CVF Conference on Computer Vision and Pattern Recognition. pp. 7132–7141. http://dx.doi.org/10.1109/CVPR.2018.00745.

Karras, T., Laine, S., Aila, T., 2019. A style-based generator architecture for generative adversarial networks. In: Proceedings of the IEEE/CVF Conference on Computer Vision and Pattern Recognition. pp. 4401–4410.

Kingma, D.P., Ba, J., 2015. Adam: A method for stochastic optimization. In: Y. Bengio, Y. LeCun (Ed.), Proc. of International Conference on Learning Representations. ICLR.

Klangbunrueang, R., Pookduang, P., Chansanam, W., Lunrasri, T., 2025. Ai-powered lung cancer detection: Assessing VGG16 and CNN architectures for CT scan image classification. Informatics 12 (1), 18.

Krizhevsky, A., Sutskever, I., Hinton, G.E., 2017. Imagenet classification with deep convolutional neural networks. Commun. ACM 60 (6), 84–90.

Kumar, S., Kumar, H., 2024. Efficient-vgg16: A novel ensemble method for the classification of covid-19 x-ray images in contrast to machine and transfer learning, procedia computer science. In: International Conference on Machine Learning and Data Engineering (ICMLDE 2023). 235, pp. 1289–1299. http://dx.doi.org/10.1016/j.procs.2024.04.122.

Lava, P., Jones, E.M., Wittevrongel, L., Pierron, F., 2020. Validation of finite-element models using full-field experimental data: Levelling finite-element analysis data through a digital image correlation engine. Strain 56 (4), e12350.

Li, Z., Liu, F., Yang, W., Peng, S., Zhou, J., 2022. A survey of convolutional neural networks: Analysis, applications, and prospects. IEEE Trans. Neural Netw. Learn. Syst. 33 (12), 6999–7019. http://dx.doi.org/10.1109/TNNLS.2021.3084827.

Liang, Z., Xu, M., Su, Y., Chen, H., Jin, G., 2024. A survey of solar panel surface defect detection methods based on improved VGG-16 model. In: 2024 IEEE 4th International Conference on Electronic Technol- ogy, Communication and Information. ICETCI, pp. 820–827. http://dx.doi.org/10.1109/ICETCI61221.2024.10594221.

Loshchilov, I., Hutter, F., 2017. Sgdr: Stochastic gradient descent with warm restarts. In: Proc. of the 5th Int. Conf. on Learning Representations. ICLR.

M. Mehdizadeh Youshanlouei, M. Rossi, 2024. Deep learning and defocus imaging for determination of three-dimensional position and orientation of microscopic objects. Phys. Fluids 36 (8).

Malowany, K., Malesa, M., Kowaluk, T., Kujawinska, M., 2017. Multi-camera digital image correlation method with distributed fields of view. Opt. Lasers Eng. 98, 198–204.

Nejjar, R., Berthon, J.-F., Garcia, J., Busto, P., Gall, J., 2023. Unsupervised domain adaptation regression by aligning inverse gram matrices. In: Proceedings of the IEEE/CVF Conference on Computer Vision and Pattern Recognition. CVPR, pp. 7484–7493.

Pan, B., Wang, B., 2020. Some recent advances in digital volume correlation. Opt. Lasers Eng. 135, 106189.

Pan, S.J., Yang, Q., 2010. A survey on transfer learning. IEEE Trans. Knowl. Data Eng. 22 (10), 1345–1359.

Peng, X., Usman, B., Kaushik, N., Hoffman, J., Wang, D., Saenko, K., 2018. Visda: A synthetic-to-real benchmark for visual domain adaptation. In: Proceedings of the IEEE Conference on Computer Vision and Pattern Recognition (CVPR) Workshops. pp. 2021–2026.

Peshave, A., Pierron, F., Lava, P., Moens, D., Vandepitte, D., 2024. Metrics to evaluate constitutive model fitness based on DIC experiments. Strain 60 (5), e12473.

Pierron, F., Grédiac, M., 2021. Towards material testing 2.0. a review of test design for identification of constitutive parameters from full-field measurements. Strain 57 (1), e12370.

Pitz, E., Rooney, S., Pochiraju, K., 2023. Estimation of spatial uncertainty in material property distributions within heterogeneous structures using optimized convolutional neural networks. Eng. Appl. Artif. Intell. 117, 105603. http://dx.doi.org/10.1016/j.engappai.2022.105603.

Reu, P.L., Toussaint, E., Jones, E., Bruck, H.A., Iadicola, M., Balcaen, R., Turner, D.Z., Siebert, T., Lava, P., Simonsen, M., 2018. DIC challenge: developing images and guidelines for evaluating accuracy and resolution of 2d analyses. Exp. Mech. 58, 1067–1099.

Rossi, M., Cortese, L., Genovese, K., Lattanzi, A., Nalli, F., Pierron, F., 2018. Evaluation of volume deformation from surface DIC measurement. Exp. Mech. 58 (7), 1181–1194.

Rossi, M., Lava, P., Pierron, F., Debruyne, D., Sasso, M., 2015. Effect of DIC spatial resolution, noise and interpolation error on identification results with the VFM. Strain 51 (3), 206–222.

Rossi, M., Pierron, F., 2012. On the use of simulated experiments in designing tests for material characterization from full-field measurements. Int. J. Solids Struct. 49 (3–4), 420–435.

Rosu, A.-M., M. Pierrot-Deseilligny, A. Delorme, Binet, R., Klinger, Y., 2015. Measurement of ground displacement from optical satellite image correlation using the free open-source software micmac. ISPRS J. Photogramm. Remote Sens. 100, 48–59.

Sarker, S., Tushar, S.N. B., Chen, H., 2023. High accuracy keyway angle identification using vgg16-based learning method. J. Manuf. Process. 98, 223–233. http://dx.doi.org/10.1016/j.jmapro.2023.04.019.

Shamshad, N., Sarwr, D., Almogren, A., Saleem, K., Munawar, A., Rehman, A.U., Bharany, S., 2024. Enhancing brain tumor classification by a comprehensive study on transfer learning techniques and model efficiency using mri datasets. IEEE Access 12, 100407–100418. http://dx.doi.org/10.1109/ACCESS.2024.3430109.

Simonyan, K., Zisserman, A., 2015. Very deep convolutional networks for large-scale image recognition. In: Proc. of the 3rd Int. Conf. on Learning Representations. ICLR.

Sun, J., Yang, F., Cheng, J., Wang, S., Fu, L., 2024. Nondestructive identification of soybean protein in minced chicken meat based on hyperspectral imaging and vgg16-svm. J. Food Comp. Anal. 125, 105713. http://dx.doi.org/10.1016/j.jfca.2023.105713.

Sutton, M.A., Orteu, J.J., Schreier, H., 2009. Image Correlation for Shape, Motion and Deformation Measurements: Basic Concepts, Theory and Applications. Springer Science & Business Media.

Szegedy, C., Liu, W., Jia, Y., Sermanet, P., Reed, S., Anguelov, D., Erhan, D., Vanhoucke, V., Rabinovich, A., 2014. Going deeper with convolutions. arXiv:1409.4842 https://arxiv.org/abs/1409.4842.

Tanoni, G., Principi, E., Mandolini, L., Squartini, S., 2022. Weakly supervised transfer learning for multi-label appliance classification. In: Mahmud, M., Ieracitano, C., Kaiser, M.S., Mammone, N., Morabito, F.C. (Eds.), Applied Intelligence and Informatics. Springer Nature Switzerland, Cham, pp. 360–375.

Tanoni, G., Stankovic, L., Stankovic, V., Squartini, S., Principi, E., 2024. Knowledge distillation for scalable nonintrusive load monitoring. IEEE Trans. Ind. Informat. 20 (3), 4710–4721. http://dx.doi.org/10.1109/TII.2023.3328436.

Trigka, M., Dritsas, E., 2025. A comprehensive survey of deep learning approaches in image processing. Sensors 25 (2), http://dx.doi.org/10.3390/s25020531.

Vermeij, T., Hoefnagels, J., 2018. A consistent full-field integrated DIC framework for hr-ebsd. Ultramicroscopy 191, 44–50.

Vermeij, T., Verstijnen, J., y Cantador, T. Ramirez, Blaysat, B., Neggers, J., Hoefnagels, J., 2022. A nanomechanical testing framework yielding front&rear-sided, high-resolution, microstructure-correlated sem-DIC strain fields. Exp. Mech. 62 (9), 1625–1646.

Wang, G., Sun, Y., Wang, J., 2017. Automatic image-based plant disease severity estimation using deep learning. In: Computational Intelligence and Neuroscience 2017.

Wang, Y., Zhou, C., 2024. Unsupervised CNN-based DIC method for 2d displacement measurement. Opt. Lasers Eng. 174, 107981.

Yadav, S.S., Jadhav, S.M., 2019. Deep convolutional neural network based medical image classification for disease diagnosis. J. Big Data 6 (1), 113.

Yosinski, J., Clune, J., Bengio, Y., Lipson, H., 2014. How transferable are features in deep neural networks?. In: Advances in Neural Information Processing Systems, Vol. 27.

Zhang, X., Zhou, X., Lin, M., Sun, J., 2017. Shufflenet: An extremely efficient convolutional neural network for mobile devices. arXiv:1707.01083 https://arxiv.org/abs/1707.01083.